# On the origin of metallic iron in eucrite breccias: Effects of impact shock and mixing on the surface of (4) Vesta

T Shisseh, H Chennaoui Aoudjehane, Roger Hewins, L Folco, Brigitte Zanda, C B Agee, Emmanuel Jacquet, L Zennouri, M H Leili, Sylvain Pont

# ON THE ORIGIN OF METALLIC IRON IN EUCRITE BRECCIAS: EFFECTS OF IMPACT SHOCK AND MIXING ON THE SURFACE OF (4) VESTA.

T. Shisseh[a, d*], H. Chennaoui Aoudjehane[a], R. Hewins[b], L. Folco[c], B. Zanda[b], C. B. Agee[d], E. Jacquet[b], L. Zennouri[a], M. H. Leili[a], S. Pont[b]

[a]Hassan II University of Casablanca, Faculty of Sciences Ain Chock, GAIA Laboratory, km 8 Route d'El Jadida 20150 Casablanca, Morocco.

[b]Institut de Minéralogie, Physique des Matériaux et Cosmochimie, MNHN and CNRS UMR 7590, CP52, 57 rue Cuvier, 75005 Paris, France.

[c]Dipartimento di Scienze della Terra, Università di Pisa, V. S. Maria 53, 56126 Pisa, Italy

[d]Institute of Meteoritics, University of New Mexico, Albuquerque, NM 87131, USA.

*Corresponding author at: Hassan II University of Casablanca, Faculty of Sciences Ain Chock, GAIA Laboratory, km 8 Route d'El Jadida 20150 Casablanca, Morocco. Tel: +212 708 031 727. *E-mail address*: shisseh.taha1@gmail.com (T. Shisseh).

## ABSTRACT

Eucrites provide important insights on the formation and the evolution of the surface and the crust of their parent body, widely believed to be the asteroid (4) Vesta. Among their minor components is metallic iron, which is not fairly described in the literature and whose formation mechanisms remain poorly understood. We performed scanning electron microscopy (SEM) and electron microprobe analysis (EPMA) investigations on the eucritic samples Errachidia 002 and Northwest Africa (NWA) 11911, with more focus on metallic iron disseminated in them, in order to constrain the processes involved in its formation, and its implications for their parent body collisional history. Errachidia 002 is a polymict eucrite that consists of basaltic and noritic (diogenite) clasts set in a fragmental matrix. Fe-metals in this meteorite contain <0.04 wt% Ni, and 0.05 wt% Co, and they are mostly associated with silica in pyroxene. This suggests their formation by decomposition of troilite, which generated S-vapors that subsequently reacted with FeO in pyroxene during an impact event, producing pure Fe-metal and silica. NWA 11911 is also a polymict eucrite composed mainly of unequilibrated and equilibrated eucritic clasts set in a clastic groundmass. Metallic iron in this breccia is either enclosed in the fragmental matrix, or within a vitrophyric impact melt clast. Its Ni and Co contents are ~2.8 and 0.6 wt%, respectively, implying a contamination by projectiles derived from an iron-bearing impactor. Our results point

out the major role impacts played in controlling the surface features and mineral compositions of early formed bodies in the solar system such as (4) Vesta.

**Keywords:** eucrite, (4) Vesta, impact processes, secondary alteration.

## GRAPHICAL ABSTRACT

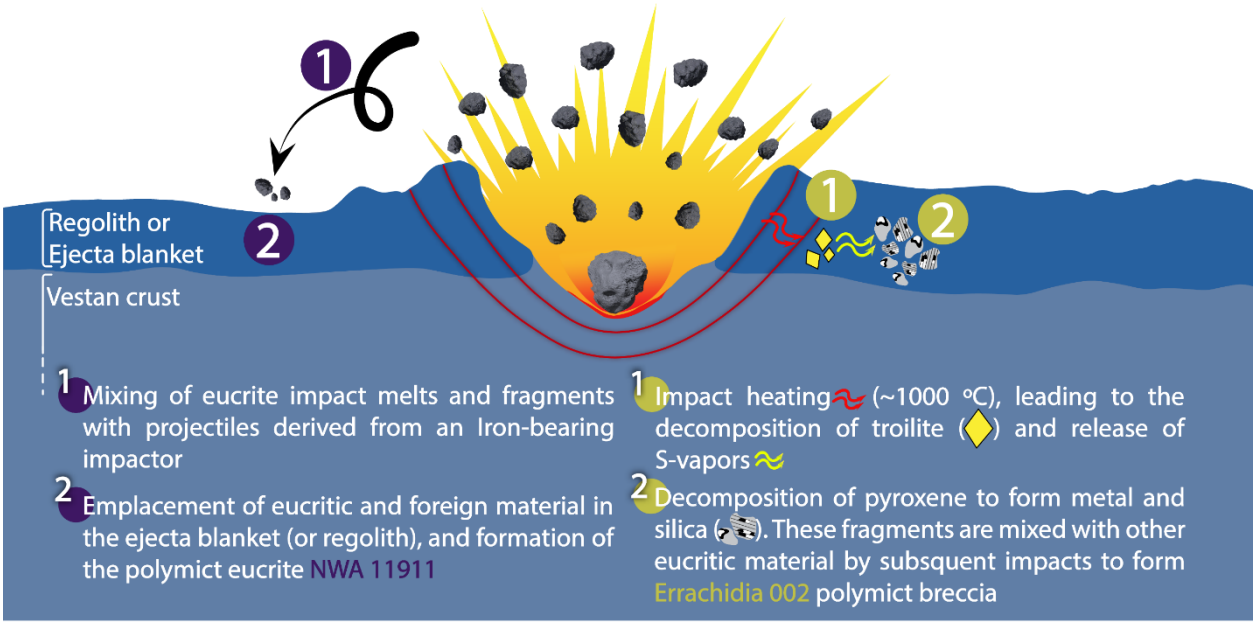


## 1. INTRODUCTION

Howardites, eucrites and diogenites (HEDs) are among the oldest igneous rocks in the solar system, and the most represented group of achondrite meteorites recovered from the surface of Earth (Roszjar et al., 2016; Hublet et al., 2017; Kleine and Wadhwa, 2017). Eucrites are either basaltic or cumulate rocks, respectively formed within the upper and lower crust of their parent body (Mittlefehldt, 2015). Diogenites are ultramafic (orthopyroxenitic, harzburgitic, dunitic, or noritic) rocks formed as plutons intruding the eucritic crust (Barrat et al., 2010; Beck and McSween, 2010; Yamaguchi et al., 2011). Howardites are rocks containing both eucrite and diogenite debris, as well as exogenous material (Duke and Silver, 1967; Lorenz et al., 2007; Unsalan et al., 2019; Jenniskens et al., 2021). These meteorites are believed to have originated from the asteroid (4) Vesta and its collisional family (i.e., vestoids), based on spectroscopic evidence from telescopic observations and Dawn spacecraft data (Binzel and Xu, 1993; Burbine et al., 2001; De Sanctis et al., 2013; McSween et al., 2013).

Eucrites record a wide array of post-crystallization processes such as widespread crustal metamorphism (Takeda and Graham, 1991; Yamaguchi et al., 1996; Yamaguchi et al., 2009; Shisseh et al., 2022), brecciation and impact mixing (Metzler et al., 1995; Kennedy et al., 2019), and various types of secondary alterations driven by S-rich or aqueous agents (Barrat et al., 2011; Zhang et al., 2013; Warren et al., 2014; Shisseh et al., 2023). Among the minor phases found in eucrites is iron metal (Duke, 1965; Mayne et al., 2009). Previous studies suggested that it formed during magmatic crystallization at reduced conditions (Duke, 1965), or by post-crystallization processes such as thermal metamorphism, contamination by iron-bearing projectiles, reduction of troilite and pyroxene during impact events, dissociation reaction of $Fe^{2+}$ in pyroxene, deposition from a FeO-rich fluid, or by troilite alteration by $H_2O$-rich fluids (Duke, 1965; Palme et al., 1988; Lorenz et al., 2007; Warren et al., 2014; Guo et al., 2021).

In this paper, we explore the petrology and the mineralogy of the eucrite breccias Errachidia 002 and NWA 11911, in order to unravel their formation history. We also examine the textures and the compositions of metallic irons found in both rocks, for the purpose of identifying their origin and implication for the post-magmatic history of the HED parent body.

## 2. METHODS

A 4.02 g piece of the polymict eucrite Errachidia 002 was recovered during a systematic prospecting mission to recover meteorites in the region of Errachidia in Morocco, in October 2017. A piece of NWA 11911 (8.9 g) was provided by Luc Labenne for classification at the Institut de minéralogie, de physique des matériaux et de cosmochimie (IMPMC), Muséum national d'Histoire naturelle (MNHN) of Paris, France. Backscattered electron (BSE) images were obtained using the scanning electron microscope TESCAN VEGAII LSU, at IMPMC (MNHN of Paris, France). X-ray elemental maps were obtained using the same system. Additional BSE images were acquired using FEI Quanta 450 ESEM FEG equipped with microanalytical energy dispersive system (EDS) Bruker QUANTAX XFlash Detector 6-10, at the Centro per la Integrazione della Strumentazione dell'University of Pisa (CISUP, Italy). Images were acquired in backscattered electron mode at an accelerating voltage of 15 kV.

The composition of the minerals was obtained using a CAMECA SX-FIVE EPMA at ISTeP (Sorbonne University in Paris, France), at an accelerating voltage of 15 kV and a beam current of 10 nA. Further analyses were performed using the JEOL 8200 Super Probe at the Institute of

Meteoritics (University of New Mexico in Albuquerque, USA). Mineral standards are: orthoclase (Al, K), apatite (P), pyrite (Fe), $Cr_2O_3$ (Cr), albite (Na), diopside (Mg, Si, Ca) and $MnTiO_3$ (Ti, Mn). The detection limits for Fe-metal analysis are: 0.04 wt % for Ni, 0.03 wt% for Fe and Co, 0.02 wt% for P, and 0.01 wt% for S.

## 3. PETROGRAPHY AND MINERAL COMPOSITION

### 3.1. ERRACHIDIA 002

Errachidia 002 consists predominately of clasts derived from various lithologies embedded in a fragmental groundmass (Fig. 1; Table 1). A backscattered electron (BSE) mosaic map of the polished section studied allowed the distinction between two lithologies (L1 and L2), separated by a network of shock veins up to 200 µm in width (see the BSE mosaic map in Fig. 1).

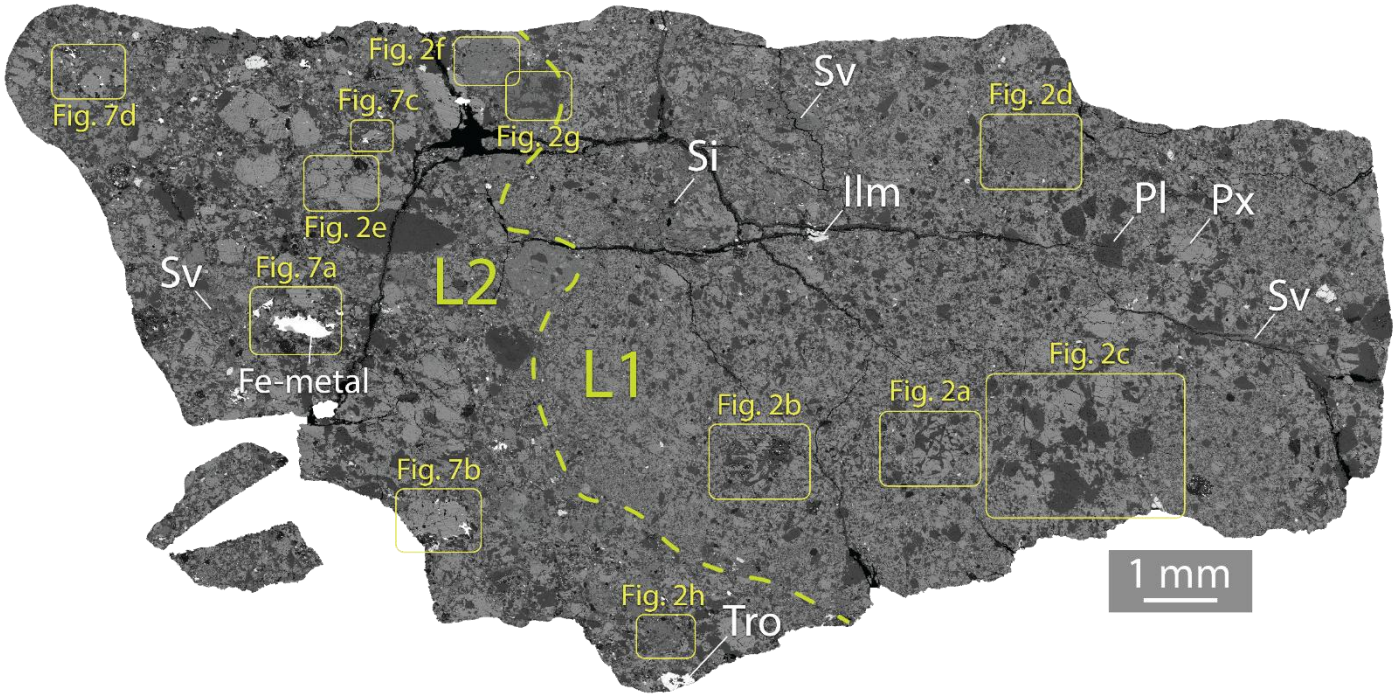


**Fig. 1.** Backscattered electron mosaic map of Errachidia 002. The dashed green line shows the limit between two lithologies; lithology 1 (L1) and lithology 2 (L2). Px = pyroxene; Pl = plagioclase; Ilm = ilmenite; Si = silica; Mx = matrix; L = lithology; Sv = shock vein.

### *3.1.1. Lithology 1 (L1)*

The first area (L1) is composed of a fragmental and locally recrystallized clastic matrix embedding subrounded to rounded basaltic, equigranular, and fine-grained clasts ranging from 0.6 to 3 mm in size (Fig. 2). The basaltic clast shown in Fig. 2a exhibits a subophitic texture, and consists of pigeonite with 5-µm-thick exsolution lamellae of augite, lath-shaped plagioclase with inclusions of pyroxene and troilite following crystallographic directions, and silica surrounded by radial cracks. The subophitic clast in Fig. 2b consists of pyroxene and plagioclase laths, as well as abundant mesostasis (silica, troilite, and ilmenite), and a few glassy shock veins with a thickness up to 20 µm intruding its margins. The clast shown in Fig. 2c is 3 mm across, which makes it the largest clast identified in L1. It has an equigranular texture overall with no mesostasis domains, and contains pyroxene and plagioclase up to 0.7 mm in diameter. We have also identified clasts composed predominately of elongated skeletal low-Ca pyroxene (60 µm in length) with random orientations, and anhedral pyroxene and plagioclase fragments, set in a fine-grained groundmass consisting of 5-µm-sized high-Ca pyroxene, plagioclase, and minor opaques (Fig. 2d).

### *3.1.2. Lithology 2 (L2)*

The second portion (L2) consists of a clastic matrix embedding basaltic, glassy, and Mg-rich diogenitic fragments. Pyroxene in the basaltic clasts is equilibrated with 25-µm-thick exsolution lamellae of augite that are mostly faulted or bended (Fig. 2e). Other phases in these clasts include plagioclase and silica (Fig. 2e). The glassy clasts are composed of mineral fragments (pyroxene, plagioclase, and silica) set in a glassy or devitrified groundmass (Fig. 2f). We found also fragments consisting mainly of BSE-dark Mg-rich pyroxene with various proportions of plagioclase and olivine (Fig. 2g, h). The matrix is crosscut by numerous glassy shock veins up to 300 µm in width, containing entrained fragments of pyroxene, plagioclase, and silica with rounded margins (Fig. 1; Fig. 2e).

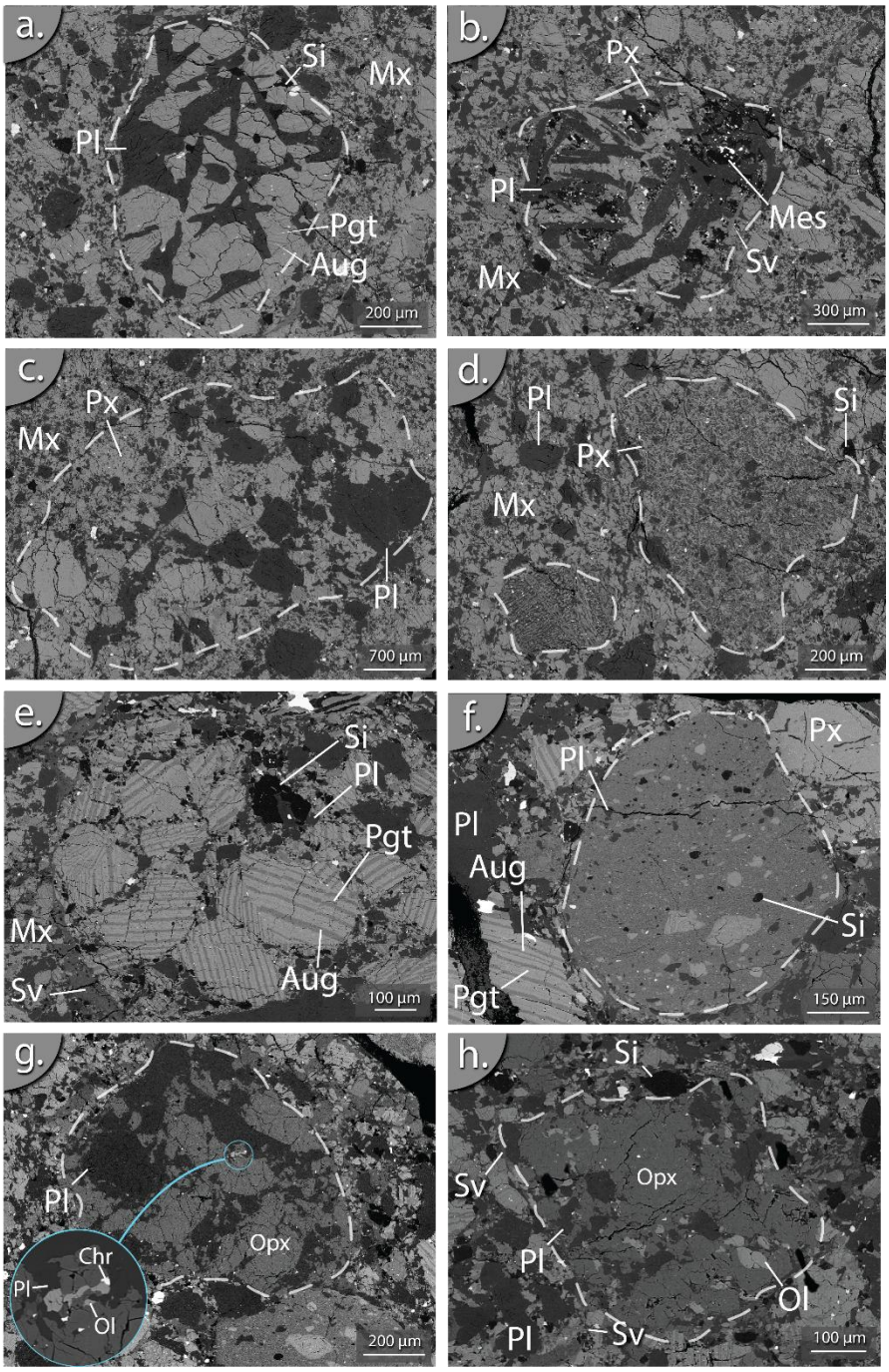


27

28 **Fig. 2.** Backscattered electron images of eucritic, glassy, and noritic diogenite clasts found in Errachidia
29 002 in lithologies 1 (a-d) and 2 (e-h). (a) subophitic basaltic clast. (b) fine-grained subophitic clast.
30 Mesostasis consists of silica, troilite, and ilmenite. (c) medium-grained, equigranular eucritic clast. (d)
31 fine-grained clast with elongated pyroxene and rounded pyroxene and plagioclase fragments set in a fine-
32 grained matrix consisting of the same mineral phases. (e) clasts with equilibrated pyroxene (with host
33 pigeonite and exsolution lamellae of augite) crystals (f) rounded glassy clast containing pyroxene and
34 silica fragments. (g, h) noritic diogenite clasts composed of Mg-rich pyroxene, plagioclase, and Mg-rich
35 olivine. Px = pyroxene; Pgt = pigeonite; Aug = augite; Ol = olivine; Pl = plagioclase; Si = silica; Chr =
36 chromite; Mes = mesostasis; Sv = shock vein.

### *3.1.3. Mineral composition*

The EPMA results and endmember compositions of pyroxene and plagioclase in Errachidia 002 are given in Table 1, and are plotted in Fig. 3a, b. In L1, the compositions of host pigeonite in the subophitic clasts in Fig. 2a and Fig. 2b range from $En_{32}Fs_{62}Wo_6$ (Mg# = [Mg/(Mg + Fe)]*100 = 35) to $En_{35}Fs_{54}Wo_{11}$ (Mg# = 39). The clast exhibiting the equigranular texture (Fig. 2c) consists of more magnesian pyroxene, with a composition of $En_{42}Fs_{55}Wo_3$ (Mg# = 43). The host pigeonite found in L2 (Fig. 2e) has a composition of $En_{35}Fs_{60}Wo_5$ (Mg# = 37), and the exsolved augite has a composition of $En_{30}Fs_{28}Wo_{42}$. The clasts shown in Fig. 2g and Fig. 2h have pyroxene with the most Mg-rich compositions in the meteorite ($En_{59\text{-}61}Wo_2$; Mg# 64), as well as plagioclase with a composition of ~$An_{95}$, and olivine with homogenous compositions of $Fo_{51\text{-}52}$. Analyzed plagioclase grains in both lithologies have a composition of $An_{93\text{-}95}$ (Fig. 3b). The glassy material in the shock veins contains 14 wt% $Al_2O_3$, 0.88 wt% $TiO_2$, 0.44 wt% $Na_2O$, and 10.8 wt% CaO.

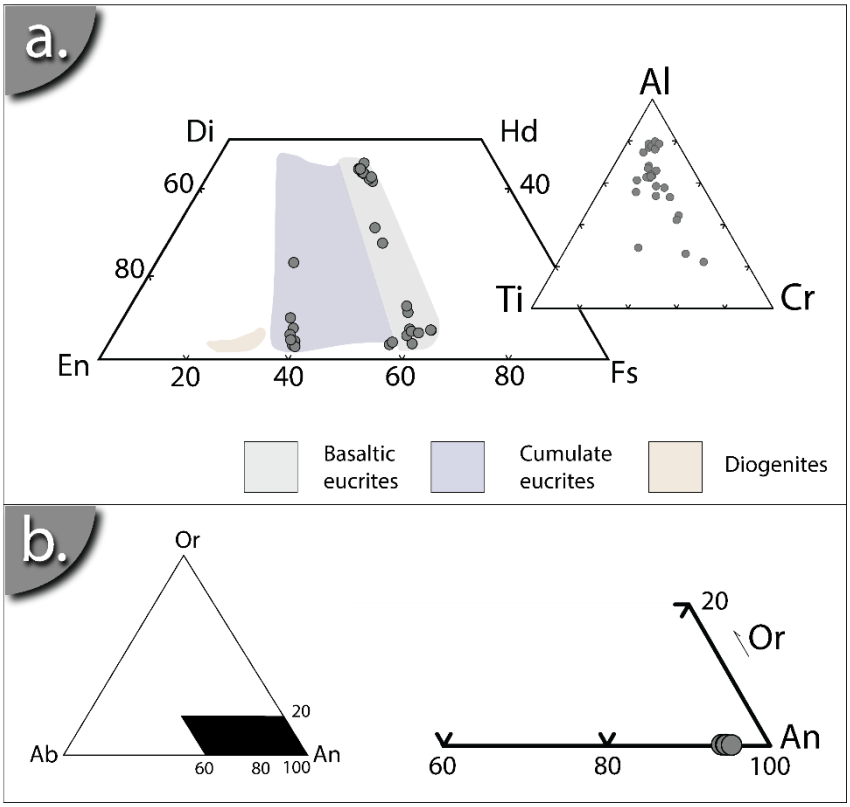


**Fig. 3.** Pyroxene (a) and plagioclase (b) endmember compositions in Errachidia 002. Compositional fields of basaltic eucrites, cumulate eucrites and diogenites are from Yamaguchi et al. (2017).

## 3.2. NWA 11911

### *3.2.1. Petrographic characteristics*

The main petrographic and geochemical characteristics of this meteorite are described in Shisseh et al. (2023). This meteorite is a polymict eucrite, as it consists of basaltic eucrite debris composed of pyroxene displaying unequilibrated and equilibrated major (Fe, Mg) and minor (Cr, Ti, Al) element compositions. The matrix of NWA 11911 contains glassy shock veins up to 80 µm in thickness embedding rounded and subrounded fragments of pyroxene, plagioclase, and silica (Fig. 5a), as well as vitrophyric impact melt clasts 1 to 5 mm across at their largest point, containing mainly skeletal and fan spherulitic pyroxenes set in a glassy groundmass (Fig. 4, Fig. 5b). The main minerals in the matrix and the clasts in NWA 11911 are pyroxene and plagioclase, with minor silica, chromite, ulvöspinel, ilmenite, troilite, ferroan olivine, and accessory Fe-Ni metal (Fig. 4).

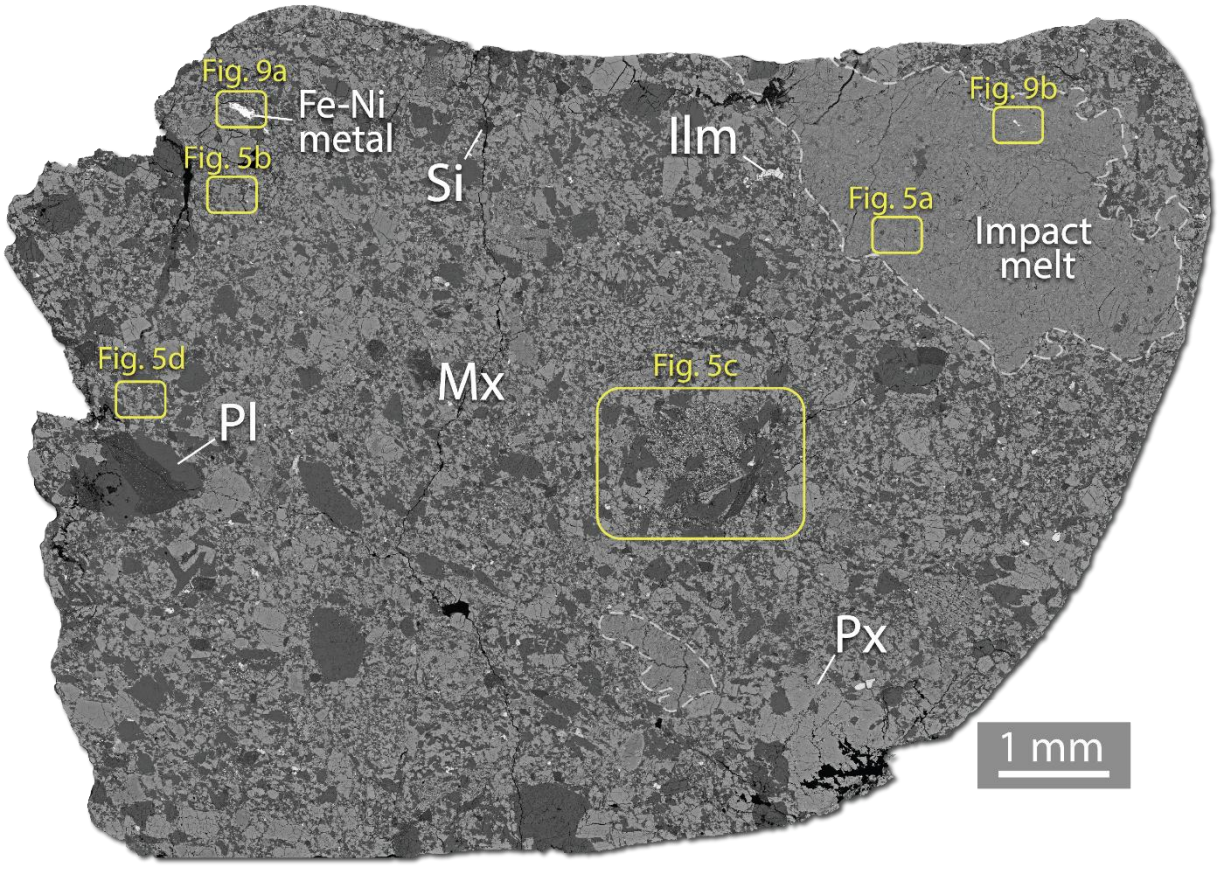


**Fig. 4.** Backscattered electron mosaic map of NWA 11911. Dashed white lines show the location of impact melt clasts embedded in the matrix. Px = pyroxene; Pl = plagioclase; Ilm = ilmenite; Si = silica; Mx = matrix.

In a recent work, we showed that NWA 11911 contains evidence of secondary alteration involving aqueous fluids, in the form of Fe-enrichment along the fractures in pyroxene, and veinlets of fayalite associated with Ca-rich secondary plagioclase, Cr-spinel, troilite, and apatite (Shisseh et al., 2023). We report the presence of two further clasts with different textures and mineralogies than the remaining eucritic clasts embedded in the matrix. The first clast, shown in Fig. 5c, is up to 1.5 mm in size and exhibits an ophitic to subophitic texture. It is mainly composed of pyroxene, plagioclase, lath-shaped silica, and ilmenite. Our observations show that most of pyroxene in this clast is replaced with a fine-grained assemblage of secondary low-Ca pyroxene, high-Ca pyroxene, silica, troilite, ilmenite with sizes ranging from 6 to 11 µm. Primary silica in the clast is porous, and contains fine troilite inclusions scattered throughout. The margins of some plagioclase grains are also invaded by these inclusions. The second clast exhibits a symplectite texture, and contains two phases of pyroxene (pigeonite and augite) with a size of 7 µm, troilite, and an intergrowth of olivine and silica (Fig. 5d).

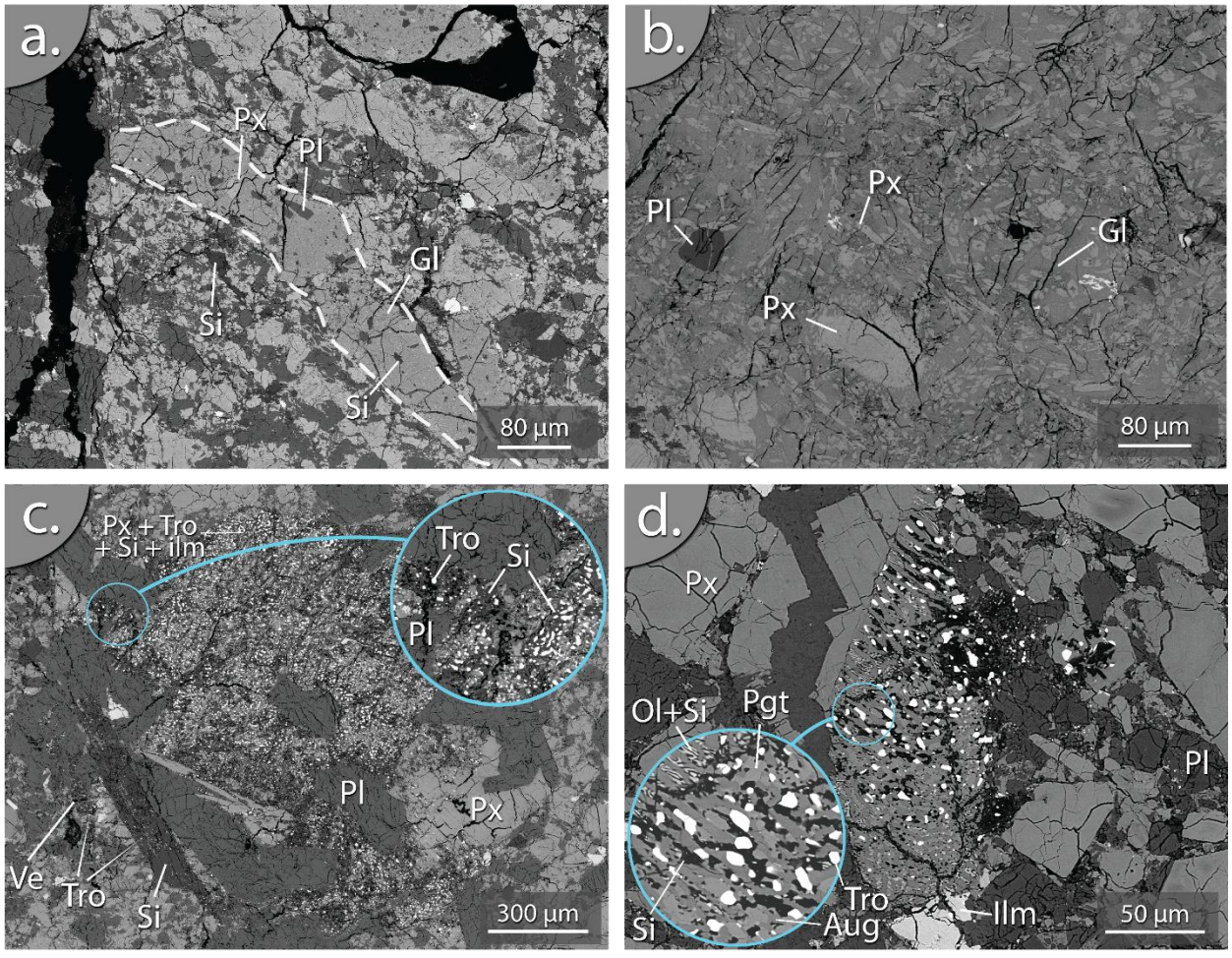

**Fig. 5.** Backscattered electron images impact products and clasts exhibiting replacement and symplectic textures in NWA 11911. (a) glassy shock vein containing entrained fragments of pyroxene, plagioclase, and silica. (b) close-up view of the impact melt clast in NWA 11911 (see upper right clast marked by dashed white line in Fig. 4). The glassy groundmass contains zoned pyroxene microlites and digested mineral fragments. (c) a subophitic clast predominately composed of pyroxene, plagioclase and lathy silica. Relict pyroxene (lower right of the image) is replaced by a fine-grained assemblage of augite, pigeonite, troilite, and silica with minor ilmenite. (d) Symplectic clast composed of vermicules and exsolutions of olivine and silica, as well as troilite and two phases of pyroxene (augite and pigeonite). Px = pyroxene; Pgt = pigeonite; Aug = augite; Ol = olivine; Pl = plagioclase; Si = silica; Tro = troilite; Ilm = ilmenite; Gl = glass; Ve = vesicle.

### *3.2.2. Mineral composition*

The average composition (± 1 standard deviation) of low-Ca pyroxene in NWA 11911 is $En_{39\pm4}Fs_{54\pm7}Wo_{7\pm6.7}$ (n = 39), and of high-Ca pyroxene is $En_{29\pm2.2}Fs_{35\pm7}Wo_{36\pm6.4}$ (Table 1; Fig. 6a). Plagioclase has a range of compositions of $An_{72\text{-}93}Ab_{6\text{-}26}Or_{1\text{-}2}$ (Table 1; Fig. 6b). The pyroxene and plagioclase grains entrained in the shock vein shown in Fig. 5a are $En_{37\text{-}39}Fs_{49\text{-}59}Wo_{2\text{-}14}$ (Fe/Mn = 31), and $An_{90\text{-}93}Ab_{5\text{-}7}$, respectively. The glass in the shock veins contains 13, 0.7, 11, 0.2 wt% of $Al_2O_3$, $TiO_2$, CaO, and $Na_2O$, respectively. Zoned pyroxene microlites in the impact melt clast in Fig. 5b display compositional ranges of $En_{42\text{-}49}Fs_{44\text{-}49}Wo_{7\text{-}9.}$ In average, The $Al_2O_3$, $TiO_2$ CaO $Na_2O$ contents of the glassy groundmass are 13.8, 0.6, 10.5, and 0.16 wt%. The relict pyroxene and the plagioclase in the clast shown in Fig. 5c have endmember compositions of $En_{33}Fs_{58}Wo_9$ (Mg# = 0.36; Fe/Mn = 32), and $An_{75\text{-}83}$ with FeO content of 0.3-0.7 wt%, respectively. The secondary phases in the pyroxene portions displaying replacement textures are augite ($En_{26\text{-}28.6}Fs_{27.9\text{-}31}Wo_{43\text{-}43.5}$ (Mg# = 0.46-0.51; Fe/Mn = 39-42), pigeonite ($En_{23.8\text{-}26.6}Fs_{43.6\text{-}48}Wo_{28.2\text{-}29.8}$ (Mg# = 0.33-0.37; Fe/Mn = 32-34), silica (96 wt% $SiO_2$) that contains 1.2 wt% FeO, ilmenite with 52 wt% $TiO_2$ and 44.6 wt% FeO, and troilite (36 wt% S; Table 1). Olivine in the symplectic assemblage in Fig. 5d is FeO-rich ($Fa_{81}$); augite is $En_{28.1}Fs_{28.4}Wo_{43.5}$ (Mg# = 0.49), and; pigeonite is $En_{33.7\text{-}35.9}Fs_{61.7\text{-}63.4}Wo_{2.4\text{-}2.9}$ (Mg# = 0.33-0.37). Silica associated with these phases contains 96 wt% $SiO_2$, and up to 1.2 wt% FeO (Table 1).

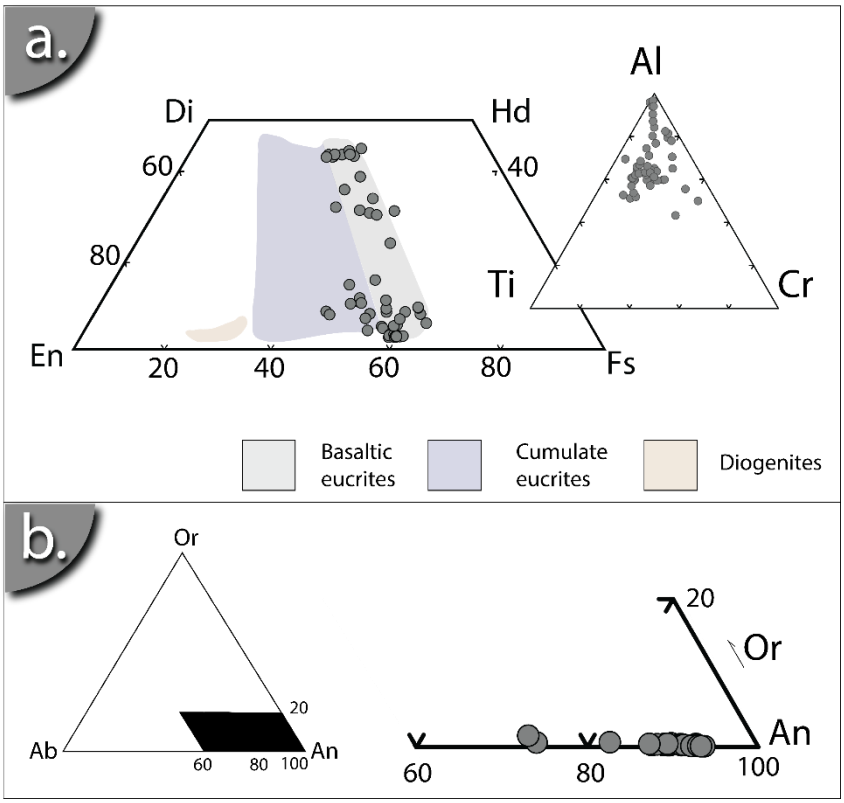


113

114 **Fig. 6.** Pyroxene (a) and plagioclase (b) endmember compositions in NWA 11911. Compositional fields
115 of basaltic eucrites, cumulate eucrites and diogenites are from Yamaguchi et al. (2017).

116

## 4. METALLIC IRON IN ERRACHIDIA 002 AND NWA 11911

### 4.1. ERRACHIDIA 002

Fe-metal in Errachidia 002 is solely present in pyroxene found in L2 (Fig. 7). EPMA data shows that the iron metal consists of very low Ni content (mostly below the detection limit of 0.04 wt%), and up to 0.05 wt% Co (Ni/Co = 0.8; Table 2). The metallic iron in the clast in Figure 7a is 800 µm in length, and contains apatite (with CaO, $P_2O_5$, FeO, F, and Cl contents of 54 wt%, 40 wt%, 2 wt%, 3.6 wt%, and 0.05 wt%, respectively), and silica grains up to 10 µm in size (see close-up images in Fig. S1). The Ca, Si, and S elemental maps of this clast (Fig. 8a) show the following: (1) augite ($En_{28}Fs_{30}Wo_{42}$) becomes abundant in the vicinity of the metal, whereas pigeonite becomes either rare or absent; (2) there is a high abundance of silica associated with the metal. This is not observed in the clasts where metal is not detected (Fig. 2e), and; (3) troilite is nearly absent in the proximity of the clast and the metal.

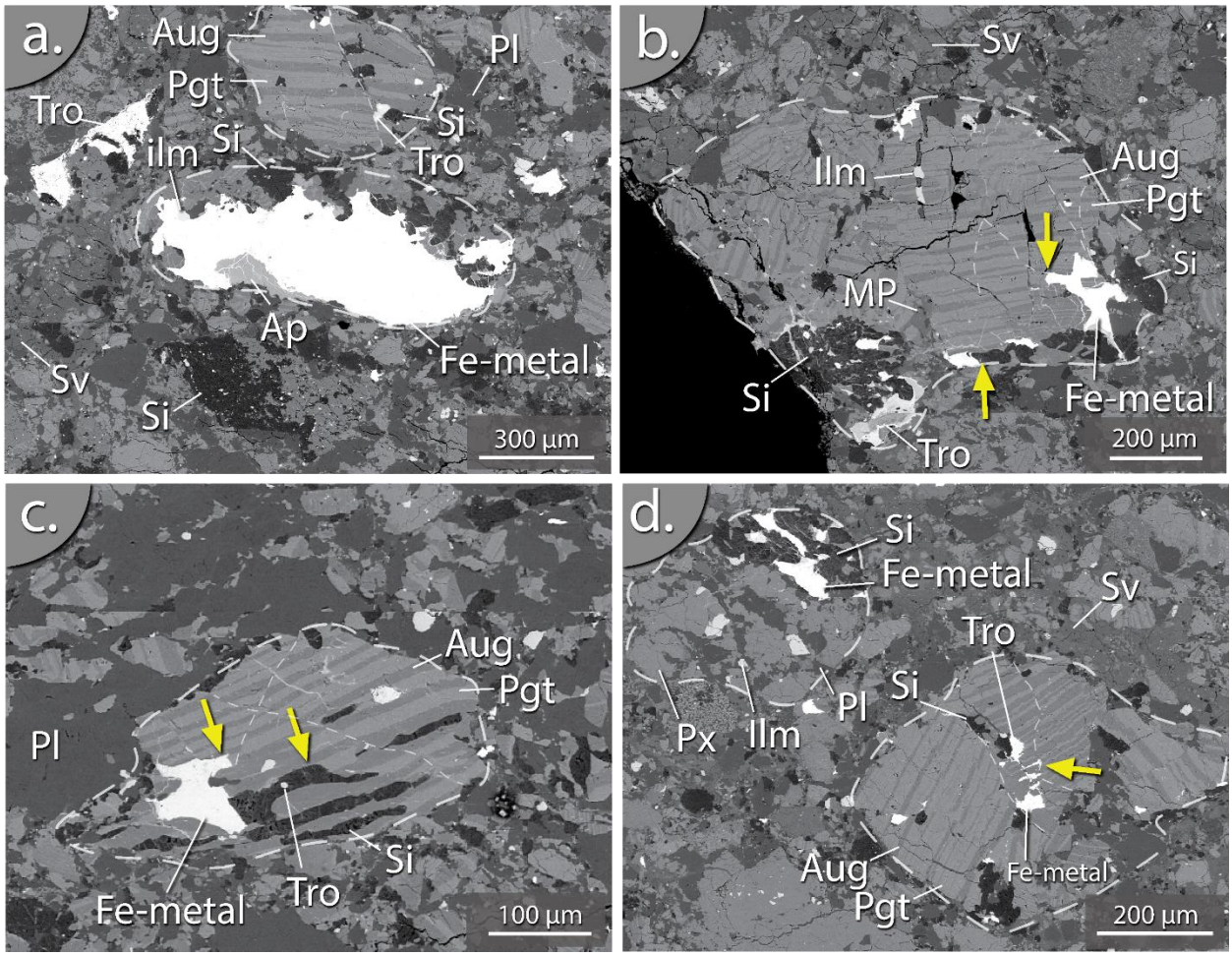


**Fig. 7.** Metallic iron in Errachidia 002. (a) Fe-metal in a pyroxene associated with silica. (b, c, d) Fe-metal in clasts composed mainly of equilibrated pyroxene with pigeonite host containing frequently bended or faulted exsolution lamellae of augite (faulting surfaces are marked with dashed lines). Associated mineral phases with Fe-metal are silica and minor troilite. Note the presence of Fe-metal and silica in a compositionally different clast (with minor to no exsolution lamellae of augite; see Fig. S1e in the supplementary material) in the upper left area in (d). X-ray elemental maps of the clast in (a) and (b) are given in Fig. 8. The yellow arrows show the protrusion of Fe-metal and silica in pigeonite, between augite exsolution lamellae. Pgt = pigeonite; Aug = augite; Pl = plagioclase; Si = silica; Ap = apatite; Ilm = ilmenite; Tro = troilite; Sv = shock vein; MP = melt pocket.

Compositionally similar iron metals were also identified in other pyroxene fragments in L2 (Fig. 7b, c, and d). The pyroxene fragment shown in Fig. 7b is equilibrated, and contains faulted and displaced exsolution lamellae of augite ranging from 3 to 14 µm in thickness (see Ca elemental maps in Fig. 8b). Silica is either associated with iron metal, or with troilite (Fe, Si and S elemental maps in Fig. 8b). In a similar way as in the clast in Fig. 7a, augite lamellae become abnormally thicker (up to 50 µm thick), and less spaced in vicinity of the metal (see Ca map in Fig. 8b, and the close-up BSE image in Fig. S1d). Another fragment of pyroxene consisting of

147 host pigeonite, displaced augite lamellae, porous silica, iron metal and troilite is shown in Fig.
148 7c. The porous silica replaces the host pigeonite, following the direction of the augite lamellae.
149 Iron metal up to 80 μm in length often protrudes the host pigeonite following the same direction.
150 Troilite is found either in host pigeonite, or as 5-μm-sized euhedral inclusions in silica. We also
151 identified comparable features in the pyroxene fragments shown in Fig. 7d, Fig. S1e and Fig.
152 S1f.

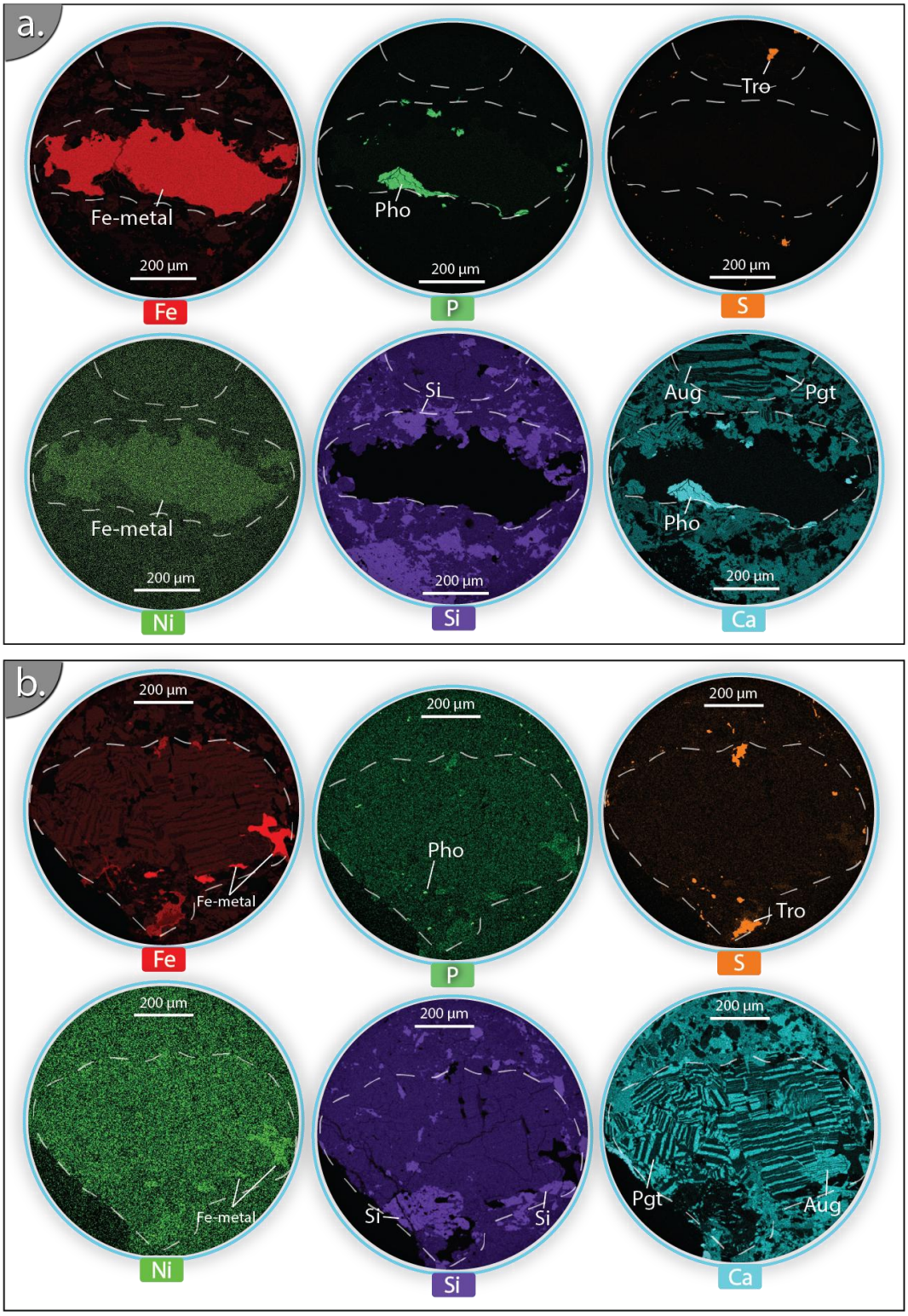


153

154 **Fig. 8.** X-ray elemental maps (Fe, Ni, P, Si, S, and Ca) of Fe-metal in Errachidia 002. The upper maps (a)
155 show the elemental distribution in the clast shown in Fig. 7a. The lower maps (b) show the elemental
156 distribution in the clast shown in Fig. 7b. Pgt = pigeonite; Aug = augite; Si = silica; Pho = phosphate; Tro
157 = troilite.

### 4.2. NWA 11911

Fe-Ni metal in NWA 11911 is found enclosed in the matrix, or in the impact melt clast (Figs. 4, 9, and 10; Fig. S2), and has an average composition of 97.5 wt% Fe, 2.8 wt% Ni, and 0.6 wt% Co (n = 5; Ni/Co = 4.2; Table 2). The metal grain (~360×100 µm) in Fig. 9a contains fragments of pyroxene (~25 µm in size), plagioclase, silica, apatite, and ilmenite (see X-ray elemental maps in Fig. 10, and close-up BSE images in Fig. S2a). The composition of low-Ca pyroxene enclosed in metal is $En_{38}Fs_{60}Wo_2$ in average (n = 4; Fe/Mn = 34), which is comparable to the composition of abutting pyroxene in the matrix ($En_{38}Fs_{59}Wo_3$; n = 4; Fe/Mn = 33.6). Plagioclase has a composition ranging from $An_{73}$ to $An_{90}$ in metal, and from $An_{78}$ to $An_{91}$ in the matrix near the metal grain. FeO and $TiO_2$ contents of ilmenite within the metal are typical of eucrite ilmenite, and are 46 wt% and 50 wt%, respectively. The apatite grains in the metal contain 55 wt% CaO, 41 wt% $P_2O_5$, and ~3 wt% FeO (see also the P elemental map in Fig. 10). Fig. 9b shows a metallic iron grain enclosed in the impact melt clast, displaying the same composition as the metal in Fig. 9a (see also Fig. S2b). Skeletal pyroxene (20 µm) in vicinity of the metal has a range of compositions of $En_{38\text{-}40}Fs_{55\text{-}58}Wo_2$, and an average Fe/Mn ratio of 33. Tiny inclusions of metal (≤ 5 µm across) are also detected in the devitrified aphanitic matrix, or within skeletal pyroxene.

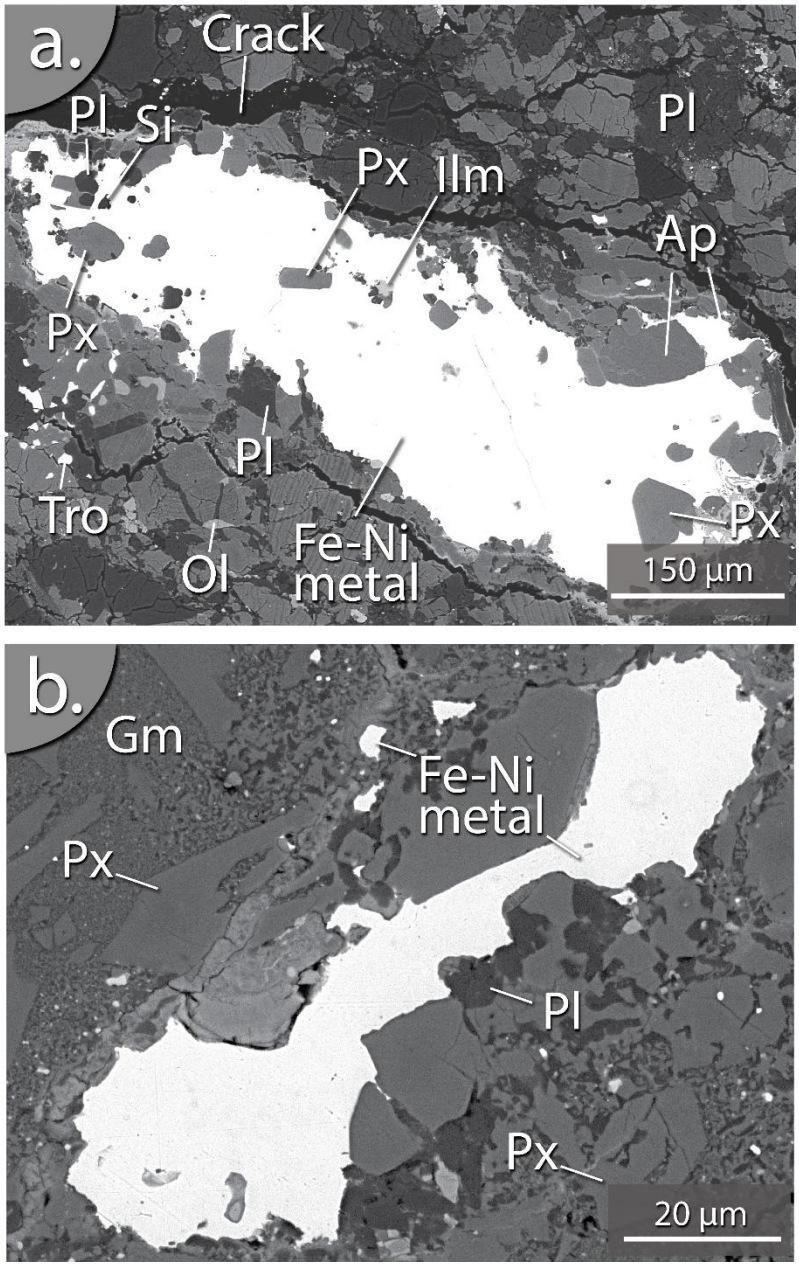


175

176 **Fig. 9.** Backscattered electron images of Fe-Ni metals found in NWA 11911. (a) Fe-Ni metal found in the
177 matrix of NWA 11911. (b) Fe-Ni metal enclosed in the impact melt clast. Close-up images of these grains
178 are presented in Fig. S2 in the supplementary material. Px = pyroxene; Pl = plagioclase; Si = silica; Ol =
179 olivine; Ap = apatite; Ilm = ilmenite; Tro = troilite; Gm = glassy and devitrified groundmass.

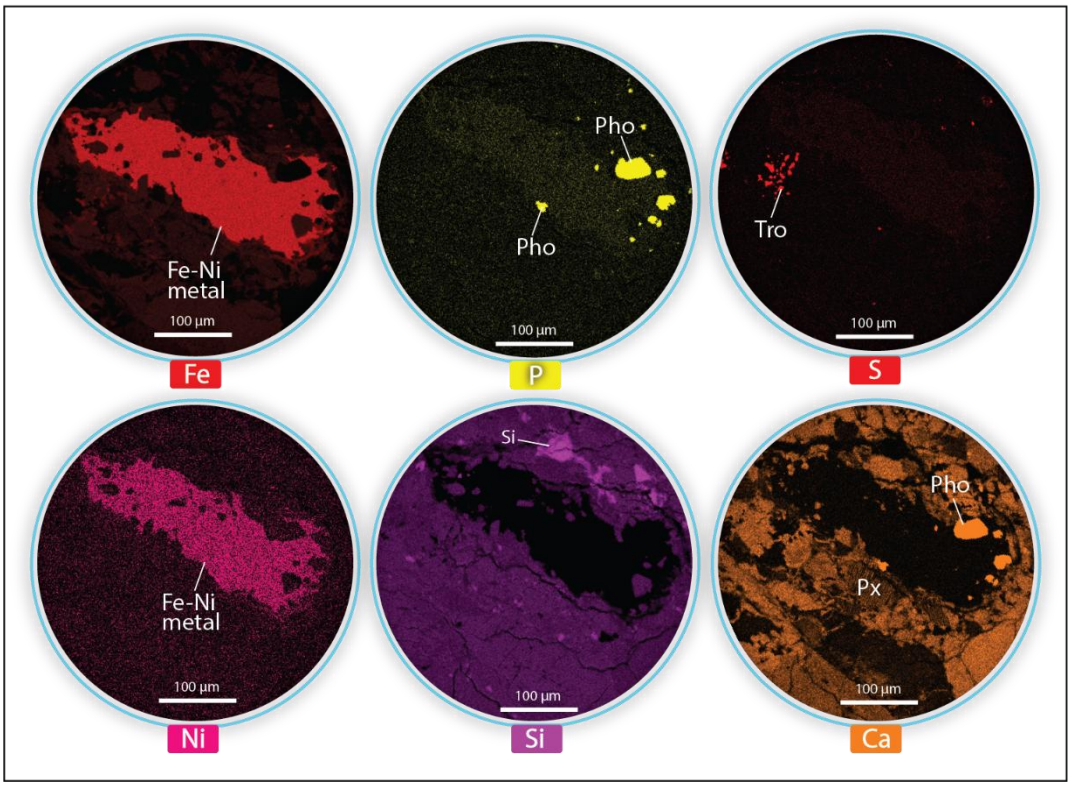


**Fig. 10.** X-ray elemental maps (Fe, Ni, P, Si, S, and Ca) of the Fe-Ni metal found in the matrix of NWA 11911, and shown in the BSE image in Fig. 9a. Px = pyroxene; Si = silica; Pho = phosphate; Tro = troilite.

# 5. DISCUSSION

## 5.1. EVIDENCE OF LITHOLOGIC MIXING BY IMPACTS IN ERRACHIDIA 002 AND NWA 11911

Unbrecciated eucrites are considered pristine (with no lithologic mixing), and are the best tool for modeling the formation and the magmatic evolution of the HED parent body (Mayne et al., 2009). On the other hand, eucrites that are brecciated, and especially those polymict (composed of two or more lithologies, with <10% diogenitic material; Delaney et al., 1983), offer a window into the collisional environment and the post-magmatic processes that controlled their parent body surface features. In this study, we examined the mineralogy and the petrology of Errachidia 002 and NWA 11911, which are two brecciated eucrites found in Morocco, in order to constrain their formation mechanisms. These rocks share a common origin as evidenced by their pyroxene Fe/Mn ratio of 31-33, which is in the range of values found in eucrites (Papike et al., 2003). This genetic link is also supported by the compositions of plagioclase found in both meteorites ($An_{72-95}$), which fall within the compositional range of eucritic plagioclase (Mittlefehldt, 2015).

### *5.1.1. Errachidia 002*

Our results show that the formation of Errachidia 002 involves multiple impact events, resulting in the excavation and the mixing of various eucritic and diogenitic lithologies. This meteorite is composed of two portions (L1 and L2; Fig. 1), each with its distinct formation history.

#### *5.1.1.1. Lithology 1 (L1)*

L1 consists of a mixture of upper crust basaltic lithologies, as well as at least one lower crust gabbroic lithology. This is supported by the textures and the major mineral compositions of the clasts investigated. The clasts in Fig. 2a and Fig. 2b are fine-grained and exhibit subophitic textures, which is consistent with the grain sizes and the textures of basaltic eucrites (Mittlefehldt, 2015). This is supported by the compositions of their pyroxene ($En_{32-35}$), which are in the range of values measured in basaltic eucrites ($En_{45-33}$; Fig. 3a; Mittlefehldt et al., 1998; Mayne et al., 2009). Pyroxene in these clasts contains exsolution lamellae of augite, implying a metamorphic event (i.e., global crustal metamorphism; Yamaguchi et al., 1996), that erased the initial igneous zoning. The effect of this event is also observed in plagioclase, which contains micron-sized exsolved inclusions that follow crystallographic directions (i.e., clouding of plagioclase; Harlow and Klimentidis, 1980). The clast shown in Fig. 2c represents a cumulate eucrite lithology, as it exhibits a coarse-grained, equigranular texture, and it is devoid of late-stage mesostasis. This is also supported by its pyroxene Mg-rich composition (Mg# = 43), which plots near the pyroxene compositional field of cumulate eucrites (Fig. 3a). The fine-grained clasts have an impact-related origin (Fig. 2d); this is evidenced by the presence of rounded eucritic fragments along with skeletal pyroxene, in the fine-grained matrix composed of plagioclase and pyroxene. Similar clasts have been identified in the Allan Hills 76005 pairing group, which formed during a process of heating and melting followed by rapid cooling of target eucritic material (Righter and Holmwood, 2020).

#### *5.1.1.2. Lithology 2 (L2)*

L2 is as well a mixture of various lithologies. The compositions of host pigeonite ($En_{35}Fs_{60}$) in the equilibrated pyroxene fragments in Fig. 2e is in the range of basaltic eucrite compositions (Mayne et al., 2009). The degree of equilibration of these pyroxene fragments are consistent with type 6 eucrites, which are characterized by a good separation between low- and high-Ca

pyroxene (Takeda and Graham, 1991). The compositions of these two phases (host pigeonite and exsolution lamellae of augite) allow the estimation of the equilibration temperature using the QUILF (quartz-ulvospinel-ilmenite-fayalite) program (Andersen et al., 1993). The equilibration temperature obtained is 732 ± 40 ºC, which is in the range of the temperatures (650-1100 °C) calculated in basaltic eucrites affected by widespread crustal metamorphism (Yamaguchi et al., 1996; Mayne et al., 2009). Evidence of impact shock and melting are present in the glassy clast in Fig. 2f; its formation is the result of superheating, followed by rapid cooling of eucritic material, as indicated by the presence of relict eucritic fragments enclosed in the glassy groundmass.

The texture, the mineralogy, and the compositions of the olivine-bearing clasts (Fig. 2g, h) suggest that they represent a ferroan noritic diogenite lithology; a transitional lithology to cumulate eucrites (Mittlefehldt, 2015) that likely formed in plutons intruding the basaltic crust. This is indicated by the following lines of evidence. (1) the presence of orthopyroxene as the dominant phase, with compositions ($En_{59-61}$) plotting in the field of cumulate eucrites ($En_{65-46}$) and slightly ferroan than pyroxene compositions in the Yamato type B noritic diogenites ($En_{64}$; Mittlefehldt, 2015) and NWA 8744 ($En_{58}$; Irving et al., 2016). (2) The presence of > 10 vol% of calcic plagioclase with an endmember composition of ~$An_{95}$, which is in the range of plagioclase compositions in cumulate eucrites, and diogenites as well ($An_{82-95.7}$; Beck and McSween, 2010). (3) the occurrence of various proportions of moderately magnesian olivine with a composition of $Fo_{51-52}$, which is comparable to the composition of olivine in the noritic diogenite NWA 8744 ($Fo_{51;}$ Irving et al., 2016), but more ferroan than olivine in the noritic diogenite NWA 8321 ($Fo_{75}$; Zhang et al., 2020). In summary, Errachidia 002 bears evidence of a complex succession of post-crystallization events such as thermal metamorphism and impacts events. The latter caused mixing of upper (basaltic) and lower (noritic diogenite) lithologies, and also enabled the formation of impact-generated features such as shock veins, as well as glassy and fine-grained clasts.

### *5.1.2. NWA 11911*

The formation history of NWA 11911 is as complex as that of Errachidia 002. This rock is composed of equilibrated and unequilibrated, monomineralic and polymineralic fragments with mineral compositions in the range of basaltic lithologies. This indicates mixing of upper crust

rocks originated from various depths given the fact that, during rapid lava eruptions on the surface of (4) Vesta, basalts that erupted first were buried and therefore metamorphosed, whereas those that erupted later were less affected by thermal metamorphism and preserved their initial igneous textures and compositions (Yamaguchi et al., 1996; Yamaguchi et al. 1997).

After and perhaps during these magmatic and metamorphic events, impact processes caused the formation of impact-engendered features such as shock veins and impact melt clasts (Fig. 5a, 5b). According to Stöffler et al. (2018), the formation of shock veins is the result of shock wave propagation during an impact event. Their presence in mafic rocks such as eucrites indicates a shock stage S4 or S5, with equilibration shock pressures up to 28 GPa or more and post-shock temperatures ranging from 200 to up to 900 ºC. The texture displayed by the dark, glassy clast embedded in the fragmental matrix of NWA 11911, and shown in Fig. 5b, could be best explained by impact melting of target eucritic rocks. Comparable dark clasts have been described in some Allan Hills 76005 paired group of eucrites by Righter and Holmwood (2020). In their work, they suggested that these clasts formed as a result of superheating and rapid cooling of surface material. This is consistent with the features observed in the impact melt clast of NWA 1191. The presence of zoned pyroxene microlites and the glassy matrix implies heating and melting of the target eucritic rocks, followed by rapid cooling (Fig. 5b). The occurrence of trapped mineral fragments with partially melted margins indicates their incorporation and reaction with the melted material prior to its cooling. These features are indicators of a shock pressure of > 55 GPa with a post-shock temperature of > 1100 ºC (see the shock metamorphism classification scheme of mafic rocks by Stöffler et al. 2018). The $Al_2O_3$, $TiO_2$, CaO, and $Na_2O$ contents of the glass in the shock vein and the impact melt clast are significantly similar, and confirm that the target rocks were mainly basaltic eucrite lithologies (Barrat et al., 2009).

Impact processes also played a major role in the formation of secondary alteration features in NWA 11911 as previously demonstrated by Shisseh et al. (2023). The formation of fractures allowed the circulation of aqueous fluids causing Fe-enrichment in pyroxene, as well as the deposition of fayalitic olivine associated with Ca-rich plagioclase, Cr-spinel, apatite, and troilite. In brief, NWA 11911 is a polymict eucrite that records multiple post-magmatic processes such as crustal thermal metamorphism, impact shock and melting, as well as fluid-assisted metasomatic reactions.

### 5.2. ORIGIN AND IMPLICATION OF METTALIC IRON IN POLYMICT EUCRITE BRECCIAS

The occurrence of Fe-metal in eucrites has been attributed to reducing magmatic conditions, post-crystallization processes engendered by thermal metamorphism, impact shock, or metasomatism (Duke, 1965; Guo et al., 2021; Lorenz et al., 2007; Palme et al., 1988; Warren et al., 2014; Shisseh et al. 2022). Based on textural and mineralogical observations, as well as the compositional data, we infer that the iron metals in the polymict eucrites Errachidia 002 and NWA 11911 have distinctly different origins.

### 5.4.1. Errachidia 002

Fe-metals in Errachidia 002 are nearly pure and contain very low Ni abundances, which rules out their origin from an exogenous impactor (see discussion below regarding Fe-Ni metal found in NWA 11911). In the plot of Ni versus Co (wt%) shown in Fig. 11, the metallic iron composition plots near the Ni-Co compositional range of pure Fe-metals found in NWA 5738, which are suggested to have formed by complex secondary alteration processes involving aqueous fluids (Warren et al., 2014). It also plots near the Ni-Co values measured in Fe-metals found in Camel Donga groundmass that are believed to be products of troilite alteration by $H_2O$-rich fluids (Warren et al., 2017).

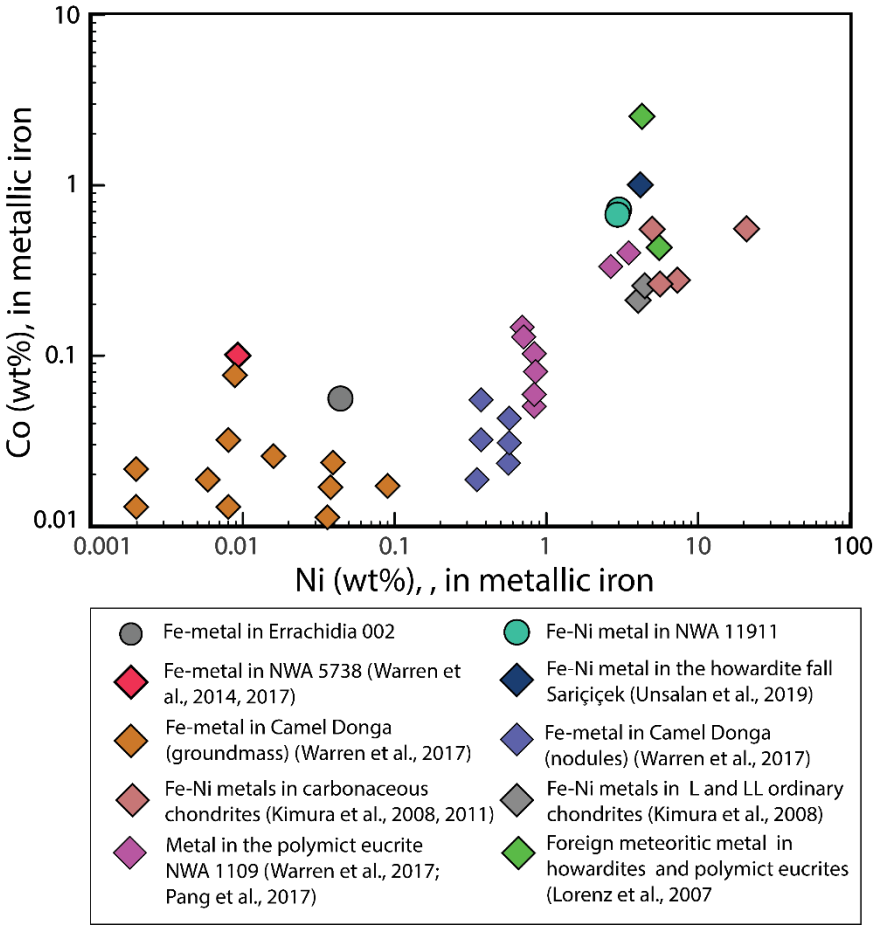


**Fig. 11.** Ni (wt%) versus Co (wt%) of iron metal in Errachidia 002 and in NWA 11911. Values measured in iron metal in chondrites, polymict eucrites, and howardites are also plotted for comparison.

Although these secondary, nearly pure Fe-metals are compositionally quite similar to metallic iron in Errachidia 002, we doubt that their formation scenarios are identical for the following reasons: (1) Fe-metals in NWA 5738 are large (up to 3.4 mm long in some cases) and are shaped like veins that cut both pyroxene and plagioclase (Warren et al., 2014). This is not observed in Errachidia 002 considering that Fe-metals are not vein-shaped, they mostly occur in individual pyroxene grains, and they do not extend to adjacent matrix or cut through any other mineral phases. Also, we did not detect any other type of secondary alteration features (fayalitic or Ca-rich plagioclase veinlets) identified by Warren et al. (2014) in NWA 5738, which constitutes further evidence that the scenario that formed the latter meteorite's Fe-metals is unlikely to explain the formation of metallic iron in Errachidia 002. (2) The formation of Fe-metals in Camel Donga groundmass likely involved the alteration of troilite by $H_2O$ fluids released by impact heating of CM-like material (Warren et al., 2017), following the reaction:

318 $3FeS + 2H_2O = 3Fe + 2H_2S + SO_2$ (Frost, 1985). This reaction is unlikely given that troilite is
319 present in some cases near Fe-metal (Fig. 7). In addition, since silica is not a by-product of this
320 reaction, it fails to explain the widespread occurrence of silica in association with Fe-metal in all
321 pyroxene grains enclosing it (Fig. 7; Fig. 8), as well as the marked replacement of FeO-rich
322 pigeonite by Fe-metal (Fig. 7).
323 To explain the formation of pure metallic iron in Errachidia 002, we suggest a mechanism
324 similar to that previously proposed by Palme et al. (1988). These authors demonstrated that an
325 increase of temperature (up to ~1000 ºC) during an impact event can cause troilite decomposition
326 and generate $S_2$ and $SO_2$ vapors. These gases will subsequently react with FeO in pyroxene to
327 produce metal and silica. In more detail, at first, heating will trigger the decomposition of troilite
328 following this reaction: $2FeS = 2Fe + S_2$ (g). Then, $S_2$ vapor will reduce more troilite and FeO in
329 pyroxene producing pure Fe-metal and silica by the reaction: $2FeSiO_3 + ½S_2 = 2Fe + 2SiO_2 +$
330 $SO_2$ (g). The production of $S_2$ and $SO_2$ in both reactions will further reduce pyroxene to metal
331 and silica. This successfully explains the following: (1) The presence of Fe-metals solely in
332 pyroxene, and more precisely in host FeO-rich pigeonite in equilibrated pyroxene grains (Fig. 7).
333 This indicates that S-vapors reacted with FeO in pyroxene to produce metal, leaving high-Ca
334 pyroxene (augite) in their vicinity. The protrusion of Fe-metal in host pigeonite (Fig. 7b, c, d;
335 Fig. S1d), but not in exsolved augite lamellae, is additional compelling evidence for this
336 selective reaction. This also implies that this process occurred after the thermal metamorphic
337 event that caused the equilibration of pyroxene, and also prior to the assembly of the breccia,
338 since iron metal is confined to clasts and is not found in the abutting matrix. (2) The reduction of
339 FeO in pyroxene would produce a great amount of silica. This is consistent with the occurrence
340 of an unusually high amount of silica in association with Fe-metal in all examined metal-bearing
341 clasts (Fig. 1; Fig. 7; Fig. 8). This process is well exemplified in Fig. 7c (see yellow arrows),
342 given that silica is replacing host pigeonite, between the exsolution lamellae of augite. (3)
343 Troilite is depleted in Fe-metal-bearing pyroxene clasts (see the S map of the large pyroxene
344 grain in the center of Fig. 8a). Yet, we detected troilite in the pyroxene clast shown in Fig. 7b
345 (see also S maps in Fig. 8b), as well as in silica and pyroxene in the form of inclusions as
346 exemplified in Fig. 7c, which indicates an incomplete decomposition reaction implying that the
347 heating event was of short duration. This was also noted by Palme et al. (1988), as they found
348 sulphide droplets in close proximity of Fe-metals in the eucrite Camel Donga.

Unlike the clasts shown in Fig. 7b, 7c, and 7d, we noted the occurrence of a large apatite grain in the Fe-metal shown in Fig. 7a. Warren et al. (2014) reported apatite in the vicinity of Fe-metal veins in NWA 5738, and suggested that this mineral phase is likely a secondary alteration product. Camel Donga's groundmass metal is also associated with apatite that occurs as clusters of 100-µm-sized grains; Warren et al. (2017) attempted to explain its formation by a process similar to that responsible of the formation of phosphates (merrillite) in mesosiderites, but eventually ruled out this scenario. Association of silica and merrillite with metal is extensively documented in mesosiderites (Harlow et al., 1982; Iannini et al., 2022; Mayne et al., 2023). The presence of these phases is well explained by a process of reduction of silicates and oxidation of P dissolved in metal (Harlow et al., 1982; Warren et al., 2017). In our case, the Fe-metal is associated with a phosphate phase as well as silica (Fig. 7a; P and Si X-ray maps in Fig. 8a), which could suggest that they formed by a similar process as that in mesosiderites. Nevertheless, there are several lines of evidence that argue against this scenario. First, Fe-metals in mesosiderites contain a significant abundance of Ni (up to ~6 wt% Ni in most cases; Wasson et al., 1974; Warren et al., 2017; Caves, 2019; Mayne et al., 2023). This is not the case in all Fe-metals found in Errachidia 002, as their Ni content is below our Ni EPMA detection limit of 0.04 wt%. Second, our EPMA analysis results from Fe-metals that do not contain a phosphate phase such as the one identified in the large metallic iron in Fig. 7a indicate that their P content is below the detection limit (<0.02 wt%), ruling out that the P that formed apatite in the large apatite-bearing Fe-metal was dissolved in it. In addition, we did not detect schreibersite, which forms in mesosiderites by exsolution of P dissolved in metal as the temperature slowly drops (Harlow et al., 1982). Finally, the oxidation product of P dissolved in mesosiderites is merrillite and not apatite. The phosphate phase found in association with the Fe-metal in Fig. 7a is apatite, and not merrillite. Nevertheless, it is important to mention that various authors (Douce et al., 2011; Sarafian et al., 2013; Warren et al., 2017) demonstrated that it is possible to form apatite from merrillite by addition of halogens.

Another mechanism that can account for the formation of apatite in Errachidia 002's pure Fe-metal is the interaction of P-vapors with Ca released from Fe-rich pigeonite during its decomposition to Fe-metal and silica. P-vapors were likely present on the surface of (4) Vesta, and their formation mechanism involved volatilization of P-bearing material as reported by Zhang et al. (2013) in the brecciated eucrite NWA 2339. According to these authors, P-vapors

reacted with Ca released from plagioclase and pyroxene after their sulfurization and subsequently formed merrillite. The apatite-metal-bearing pyroxene clast in Errachidia 002 (Fig. 7a) is basaltic in composition, and late-stage mesostasis in eucritic basalts consists mostly of late-stage phases such as phosphates (mainly apatite) and troilite (Patzer and McSween, 2012), which could be a great source of P- and S-vapors when heated during a high energetic impact. The distribution of mesostasis in eucrites is also heterogenous. This could explain why there is a substantial amount of Fe-metal, silica, and apatite in that particular grain (Fig. 7a) and not in the others (Fig. 7b, c, d; Fig. S1e, f), as nearby mesostasis-rich areas were heated to produce abundant S-vapors that reacted with FeO in pyroxene to form pure Fe-metal and silica, as well as P-bearing vapors that combined with Ca released from pyroxene to form apatite. Note that an origin of these vapors from the impactor itself cannot be ruled out entirely.

#### 5.4.2. NWA 11911

Eucrites contain usually metal with low Ni content (<0.01-0.1 wt% Ni; Yamaguchi et al., 2006), as the majority of nickel has segregated into the metallic core of their parent body. The metal in NWA 11911 has 2.8 wt% Ni, and plots in the Ni-Co field of metals found in chondrites, as well as foreign metals in polymict eucrites and howardites (Fig. 11). This provides a strong indication of contamination by projectiles, most likely derived from a nearby impact event involving a metal-bearing impactor. This collision caused fragmentation and melting of eucritic rocks, followed by their mixing with exogenous metal projectiles, as indicated by the presence of minerals with compositions in the range of eucrite mineral phases incorporated in the Fe-Ni metal (Fig. 9a), and the presence of metal in the impact melt clast with a glassy matrix displaying compositions consistent with basaltic eucrite target rocks (Fig. 9b).

### 5.5. FORMATION OF FINE-GRAINED ASSEMBLAGES IN NWA 11911

A few clasts in NWA 11911 exhibit distinct textures and mineralogies compared to the monomineralic and polymineralic basaltic clasts found in the matrix. The clast shown in Fig. 5c displays a sulfide-rich fine-grained texture, marked by the presence of an assemblage of Fe-rich pigeonite, Mg-rich augite, silica, troilite, and ilmenite. Note that these assemblages are only found in pyroxene, and do not occur in plagioclase. Typically, one would think that these are mesostasis areas given that some of these phases (mainly silica, troilite, and ilmenite) are among

the latest mineral phases to crystallize in a eucritic magma (Yamaguchi et al., 2009). This interpretation is unlikely considering that mesostasis areas in eucrites are usually dominated by silica, and their shape is controlled by the surrounding early-formed mineral phases (Mayne et al., 2009; Shisseh et al., 2022). The presence of subequal amount of troilite and silica, as well as the presence of two fine-grained pyroxene phases with differently distinct compositions ($En_{26-28}Wo_{43-43.5}$ and $En_{23.8-26.6}Wo_{28.2-29.8}$) than Fe-rich host pyroxene ($En_{33}Wo_{9}$) implies a mechanism of pyroxene sulfurization by S-vapors. Similar process was described by Zhang et al. 2013 in NWA 2339. According to these authors, dry S-vapors formed by volatilization of S-bearing material on the surface (4) Vesta are responsible for the formation of secondary minerals that replace primary Fe-rich pyroxene, such as Mg-rich augite, Mg-rich ferrosilite, silica, troilite and ilmenite. Another plausible effect of sulfurization includes the occurrence of vesicles and inclusions of troilite in silica (see lower left corner in Fig. 5c). Sulfurization of eucritic silica was described in the monomict basaltic eucrite NWA 11591, resulting in SRTs (sulfide-rich replacement textures) with porous regions composed of quartz and troilite along the fractures and rims (Huang et al., 2020). These authors explained the formation of troilite by a reaction of S-vapors with FeO transported by S-vapors from pyroxene or Fe-rich mesostasis, or with metallic Fe.

The texture and mineral assemblage (two pyroxene phases, silica, and troilite) observed in the lithic clast shown in Fig. 5d is considerably similar to what we described above. However, some differences arise such as the presence of Fe-rich olivine ($Fa_{81}$) associated with silica in the form of lamellae and vermicules, as well as the fact that they display a sharp boundary with host pyroxene. This suggests that this clast is a symplectite formed by cooling of melts (Rasmussen et al., 2008), or reheating by magmatic intrusions or during impact events (Barrat et al. 2012). Symplectites showing similar textures and mineralogies have been previously described in terrestrial rocks, HED meteorites, lunar meteorites, and Martian meteorites (Aramovich et al., 2002; Liu et al., 2009; Patzer and McSween, 2012). To explain their formation, Rost et al. (2009) invoked a mechanism involving the breakdown of pyroxferroite, which occurred under rapid cooling and at low pressures. The presence of this symplectic clast in NWA 11911 provides evidence that Fe-rich evolved eucritic lithologies exist on (4) Vesta, in a similar way as other planetary objects such as Earth, the Moon, and Mars.

## CONCLUSION

Errachidia 002 and NWA 11911 are eucrite finds recovered in Morocco. Both rocks are polymict as they consist of fragments originated from various upper and lower crust lithologies. Errachidia 002 is characterized by the presence of two lithologies consisting of basaltic, cumulate, and noritic diogenite debris. NWA 11911 is composed mainly of unequilibrated and equilibrated basaltic fragments, as well as some impact-generated features like shock veins and impact melts. Both rocks consist of a fragmental matrix with fine-grained fragments of typical eucrite minerals.

We investigated metallic irons found in Errachidia 002 and NWA 11911 to determine their origin and their implication for the collisional history of the eucrite parent body. Our results show that Fe-metals in Errachidia 002 solely occur in pyroxene, and are characterized by very low Ni and Co contents. Their formation is most likely the result of heating during a highly energetic impact event of short duration that caused the decomposition of troilite, resulting in the production of S-vapors, which subsequently reacted with FeO in pyroxene to form metal and silica. The presence of apatite in one of the Fe-metal grains plausibly indicate the reaction of P-vapors generated by volatilization of P-bearing material (likely mesostasis areas) with Ca released by pyroxene during its decomposition. The Fe-Ni metal in NWA 11911 has a different origin and is from a foreign meteoritic source, as indicated by its elevated Ni and Co contents. This metal was most likely emplaced during an impact event of a metal-bearing impactor with (4) Vesta, which caused mixing of both its metal with fragments and impact melts of target basaltic eucrite rocks.

We demonstrated in a previous work that NWA 11911 contains evidence of Fe-metasomatic features engendered by aqueous fluids. In this study, we showed that it also contains records of secondary alteration by S-vapors, resulting in a sulphide-rich replacement texture engendered by the decomposition of Fe-rich pyroxene. It also contains clasts originated from an evolved lithology, displaying symplectic textures formed by the breakdown of metastable pyroxene. The presence of both types of secondary alteration in the same meteorite, as well as symplectic clasts makes NWA 11911 an unprecedented eucritic sample providing a window into the complex magmatic and post-magmatic history of its parent body.

In conclusion, our findings from the polymict eucritic breccias Errachidia 002 and NWA 11911 shed light on the important role impacts played in the surface evolution of planetary bodies like the asteroid (4) Vesta.

## ACKNOWLEDGEMENT

The analyses performed at the Natural History Museum of Paris in France, and the University of Pisa in Italy were funded by the Erasmus+ program. The analyses performed at the Institute of Meteoritics (University of New Mexico) were funded by the Fulbright joint supervision program. We greatly appreciate the assistance of Michael Spilde (IOM, University of New Mexico, USA), Randa Ishak (CISUP, Università di Pisa, Italy), and Andrea Risplendente (UNITECH, Università di Milano, Italy) during the SEM and EPMA sessions.

## REFERENCES


Andersen, D. J., Lindsley, D. H., and Davidson, P. M. (1993). QUILF: a pascal program to assess equilibria among Fe-Mg-Mn-Ti oxides, pyroxenes, olivine, and quartz. Computers and Geosciences 19, 1333–1350.

Aramovich, C. J., Herd, C. D. K., and Papike, J. J. (2002). Symplectites derived from metastable phases in Martian basaltic meteorites. American Mineralogist 87, 1351–1359. https://doi.org/10.2138/AM-2002-1010

Barrat, J. A., Bohn, M., Gillet, P., and Yamaguchi, A. (2009). Evidence for K-rich terranes on Vesta from impact spherules. Meteoritics and Planetary Science 44, 359–374. https://doi.org/10.1111/j.1945-5100.2009.tb00738.x

Barrat, J. A., Yamaguchi, A., Zanda, B., Bollinger, C., and Bohn, M. (2010). Relative chronology of crust formation on asteroid Vesta: Insights from the geochemistry of diogenites. Geochimica et Cosmochimica Acta 74, 6218–6231. https://doi.org/10.1016/j.gca.2010.07.028

Barrat, J. A., Yamaguchi, A., Bunch, T. E., Bohn, M., Bollinger, C., and Ceuleneer, G. (2011). Possible fluid-rock interactions on differentiated asteroids recorded in eucritic meteorites. Geochimica et Cosmochimica Acta 75, 3839–3852. https://doi.org/10.1016/j.gca.2011.04.013

Barrat, J. A., Yamaguchi, A., Jambon, A., Bollinger, C., and Boudouma, O. (2012). Low-Mg rock debris in howardites: Evidence for KREEPy lithologies on Vesta? Geochimica et Cosmochimica Acta 99, 193–205. https://doi.org/10.1016/j.gca.2012.09.026

Beck, A. W., and McSween, H. Y. (2010). Diogenites as polymict breccias composed of orthopyroxenite and harzburgite. Meteoritics and Planetary Science 45, 850–872. https://doi.org/10.1111/j.1945-5100.2010.01061.x

Binzel R. P. and Xu S. (1993). Chips off asteroid 4 Vesta: Evidence for the parent body of basaltic achondrite meteorites. Science 260, 186–191.

Burbine, T. H., Buchanan, P. C., Binzel, R. P., Bus, S. J., Hiroi, T., Hinrichs, J. L., Meibom, A., and McCoy, T. J. (2001). Vesta, Vestoids, and the howardite, eucrite, diogenite group: Relationships and the origin of spectral differences. Meteoritics and Planetary Science 36, 761–781. https://doi.org/10.1111/j.1945-5100.2001.tb01915.x

Caves, L. R. (2019). Mesosiderite Formation: Redox from the Metal Perspective. MPhil Thesis, Texas Christian University, Fort Worth, TX, USA.

De Sanctis M. C., Ammannito E., Capria M. T., Capaccioni F., Combe J.-P., Frigeri A., Magni G., Marchi S., McCord T. B., Palomba E., Tosi F., Zambon F., Carraro F., Fonte S., McFadden L. A., Mittlefehldt D. W., Pieters C. M., Jaumann R., Stephan K., Raymond C. A., and Russell C. T. (2013). Vesta's mineralogical composition as revealed by VIR on Dawn. Meteoritics and Planetary Science, doi:10.1111/maps.12138.

Delaney, J. S., Takeda, H., Prinz, M., Nehru, C. E., and Harlow, G. E. (1983). The nomenclature of polymict basaltic achondrites. Meteoritics 18, 103–111. https://doi.org/10.1111/j.1945-5100.1983.tb00581.x

Duke, M. B. (1965). Metallic iron in basaltic achondrites. Journal of Geophysical Research, 70, 1523–1529.

Duke, M. B., and Silver, L. T. (1967). Petrology of eucrites, howardites and mesosiderites. Geochimica et Cosmochimica Acta 31, 1637–1665. https://doi.org/10.1016/0016-7037(67)90112-3

Frost, B. R. (1985). On the Stability of Sulfides, Oxides, and Native Metals in Serpentinite. Journal of Petrology 26, 31–63. https://doi.org/10.1093/PETROLOGY/26.1.31

Guo, Z., Li, Y., Chen, H., Zhang, M., Wu, Y., Hui, B., Liu, S., Coulson, I. M., Li, S., Li, X., Liu, J., and Ouyang, Z. (2021). Evidence for the Disproportionation of Iron in a Eucrite Meteorite: Implications for Impact Processes on Vesta. Journal of Geophysical Research: Planets 126, e2020JE006816. https://doi.org/10.1029/2020JE006816

Harlow, G. E., and Klimentidis, R. (1980). Clouding of pyroxene and plagioclase in eucrites - Implications for post-crystallization processing. 11th Lunar and Planetary Science Conference, pp. 1131–1143. https://doi.org/10.1017/CBO9781107415324.004

Harlow, G. E., Delaney, J. S., Nehru, C. E., and Prinz, M. (1982). Metamorphic reactions in mesosiderites: origin of abundant phosphate and silica. Geochimica et Cosmochimica Acta 46, 339–348. https://doi.org/10.1016/0016-7037(82)90225-3

Huang L.-L., Miao B.-K., Chen G.-Z., Shao H.-M., and Ouyang Z.-Y. (2020). The sulfurization recorded in tridymite in the monomict eucrite Northwest Africa 11591. Meteoritics and Planetary Science 55, 1441–1457.

Hublet, G., Debaille, V., Wimpenny, J., and Yin, Q. Z. (2017). Differentiation and magmatic activity in Vesta evidenced by 26Al-26Mg dating in eucrites and diogenites. Geochimica et Cosmochimica Acta 218, 73–97. https://doi.org/10.1016/j.gca.2017.09.005

Iannini Lelarge, S., Folco, L., Masotta, M., Greenwood, R. C., Russell, S. S., and Bates, H. C. (2022). Asteroids accretion, differentiation, and break-up in the Vesta source region: Evidence from cosmochemistry of mesosiderites. Geochimica et Cosmochimica Acta 329, 135–151. https://doi.org/10.1016/J.GCA.2022.05.003

Irving, A. J., Kuehner, S. M., Wittke, J. H., Tait, K. T., Irving, A. J., Kuehner, S. M., Wittke, J. H., and Tait, K. T. (2016). Noritic Diogenites and Feldspathic Diogenites: Evolved Ancient Cumulates Potentially Related to Mesosiderites and Not to Any Eucrites. 47th Lunar and Planetary Science Conference. LPI Contribution No. 1903.

Jenniskens, P., Gabadirwe Yin, Q.-Z. M., Proyer, A., Moses, O., Kohout, T., Franchi, F., Gibson, R. L., et al. (2020). Impact and Recovery of Asteroid 2018 LA. Meteoritics and Planetary Science 56, 844–93. https://doi.org/10.1111/maps.13653

Kennedy, T., Jourdan, F., Eroglu, E., and Mayers, C. (2019). Bombardment history of asteroid 4 Vesta recorded by brecciated eucrites: Large impact event clusters at 4.50 Ga and discreet bombardment until 3.47 Ga. Geochimica et Cosmochimica Acta 260, 99–123. https://doi.org/10.1016/J.GCA.2019.06.027

Kleine, T., and Wadhwa, M. (2017). Chronology of planetesimal differentiation. In Planetesimals: Early Differentiation and Consequences for Planets. Cambridge University Press. pp. 224–245 https://doi.org/10.1017/9781316339794.011

Liu, Y., Floss, C., Day, J. M. D., Hill, E., and Taylor, L. A. (2009). Petrogenesis of lunar mare basalt meteorite Miller Range 05035. Meteoritics and Planetary Science 44, 261–284. https://doi.org/10.1111/J.1945-5100.2009.TB00733.X

Lorenz, K. A., Nazarov, M. A., Kurat, G., Brandstaetter, F., and Ntaflos, Th. (2007). Foreign meteoritic material of howardites and polymict eucrites. Petrology 15, 109–125. https://doi.org/10.1134/S0869591107020014

Mayne, R. G., McSween, H. Y., McCoy, T. J., and Gale, A. (2009). Petrology of the unbrecciated eucrites. Geochimica et Cosmochimica Acta 73, 794–819. https://doi.org/10.1016/j.gca.2008.10.035

Mayne, R. G., Caves, L., McCoy, T. J., Ash, R. D., and McDonough, W. F. (2023). Metal in mesosiderites: Evidence for redox and fractional crystallization. Meteoritics and Planetary Science 58, 1211–1228. https://doi.org/10.1111/MAPS.14031

McSween, H. Y., Binzel, R. P., De Sanctis, M. C., Ammannito, E., Prettyman, T. H., Beck, A. W., Reddy, V., Le Corre, L., Gaffey, M. J., Mccord, T. B., Raymond, C. A., and Russell, C. T. (2013). Dawn; the Vesta-HED connection; and the geologic context for eucrites, diogenites, and howardites. Meteoritics and Planetary Science 48, 2090–2104. https://doi.org/10.1111/maps.12108

Metzler, K., Bobe, K. D., Palme, H., Spettel, B., and Stöffler, D. (1995). Thermal and impact metamorphism on the HED parent asteroid. Planetary and Space Science 43, 499–525. https://doi.org/10.1016/0032-0633(94)00219-H

Mittlefehldt, D. W., McCoy, T. J., Goodrich, C. A., and Kracher, Alfred. (1998). Non-chondritic meteorites from asteroidal bodies. Planetary Materials, 1988, 4-001-4–196. https://doi.org/10.1007/978-1-59745-060-7

Mittlefehldt, D. W. (2015). Asteroid (4) Vesta: I. The howardite-eucrite-diogenite (HED) clan of meteorites. Chemie Der Erde - Geochemistry 75, 155–183. https://doi.org/10.1016/j.chemer.2014.08.002

Palme, H., Wlotzka, F., Spettel, B., Dreibus, G., and Weber, H. (1988). Camel Donga: A Eucrite with High Metal Cnotent. Meteoritics 23, 49–57. https://doi.org/10.1111/j.1945-5100.1988.tb00896.x

Papike, J. J., Karner, J. M., and Shearer, C. K. (2003). Determination of planetary basalt parentage: A simple technique using the electron microprobe. American Mineralogist 88, 469–472.

Patiño Douce, A. E., Roden, M. F., Chaumba, J., Fleisher, C., and Yogodzinski, G. (2011). Compositional variability of terrestrial mantle apatites, thermodynamic modeling of apatite volatile contents, and the halogen and water budgets of planetary mantles. Chemical Geology 288, 14–31. https://doi.org/10.1016/j.chemgeo.2011.05.018

Patzer, A., and McSween jr., H. Y. (2012). Ordinary (mesostasis) and not-so-ordinary (symplectites) late-stage assemblages in howardites. Meteoritics and Planetary Science 4, 1475–1490. https://doi.org/10.1111/j.1945-5100.2012.01408.x

Rasmussen, B., Fletcher, I. R., and Muhling, J. R. (2008). Pb/Pb geochronology, petrography and chemistry of Zr-rich accessory minerals (zirconolite, tranquillityite and baddeleyite) in mare basalt 10047. Geochimica et Cosmochimica Acta 72, 5799–5818. https://doi.org/10.1016/J.GCA.2008.09.010

Righter, K., and Holmwood, A. P. (2020). Mineralogy and petrology of dark clasts in the Allan Hills 76005 polymict eucrite pairing group. Meteoritics and Planetary Science 55, 781–799. https://doi.org/10.1111/MAPS.13465

Rost, D., Stephan, T., Greshake, A., Fritz, J., Weber, I., Jessberger, E. K., and Stöffler, D. (2009). A combined ToF-SIMS and EMP/SEM study of a three-phase symplectite in the Los Angeles basaltic shergottite. Meteoritics and Planetary Science 44, 1225–1237. https://doi.org/10.1111/J.1945-5100.2009.TB01219.X

Roszjar, J., Whitehouse, M. J., Srinivasan, G., Mezger, K., Scherer, E. E., Van Orman, J. A., and Bischoff, A. (2016). Prolonged magmatism on 4 Vesta inferred from Hf–W analyses of eucrite zircon. Earth and Planetary Science Letters 452, 216–226. https://doi.org/10.1016/J.EPSL.2016.07.025

Sarafian, A. R., Roden, M. F., and Patiño-Douce, A. E. (2013). The volatile content of Vesta: Clues from apatite in eucrites. Meteoritics and Planetary Science 48, 2135–2154. https://doi.org/10.1111/maps.12124

Shisseh, T., Chennaoui Aoudjehane, H., Agee, C. B., and Boudouma, O. (2022). Tirhert and Aouinet Legraa: Rare unbrecciated eucrite falls. Meteoritics and Planetary Science 57, 1920–1935. https://doi.org/10.1111/MAPS.13899

Shisseh, T., Chennaoui Aoudjehane, H., Barrat, J. A., Zanda, B., Hewins, R. H., Agee, C., Folco, L., Jacquet, E., and Pont, S. (2023). Fluid-assisted metasomatic processes on planetary bodies: Evidence from vestan lithologies. Geochimica et Cosmochimica Acta 340, 51–64. https://doi.org/10.1016/J.GCA.2022.11.007

Stöffler, D., Hamann, C., and Metzler, K. (2018). Shock metamorphism of planetary silicate rocks and sediments: Proposal for an updated classification system. Meteoritics and Planetary Science 53, 5–49. https://doi.org/10.1111/MAPS.12912

Takeda, H., and Graham, a L. (1991). Degree of equilibration of eucritic pyroxenes and thermal metamorphism of the earliest planetary crust. Meteoritics 26, 129–134. https://doi.org/10.1111/j.1945-5100.1991.tb01028.x

Unsalan, O., Jenniskens, P., Yin, Q. Z., Kaygisiz, E., Albers, J., Clark, D. L., Granvik, M., Demirkol, I., Erdogan, I. Y., Bengu, A. S., Özel, M. E., Terzioglu, Z., Gi, N., Brown, P., Yalcinkaya, E., Temel, T., Prabhu, D. K., Robertson, D. K., Boslough, M., et al. (2019). The Sariçiçek howardite fall in Turkey: Source crater of HED meteorites on Vesta and impact risk of Vestoids. Meteoritics and Planetary Science 54, 953–1008. https://doi.org/10.1111/maps.13258

Warren, P. H., Rubin, A. E., Isa, J., Gessler, N., Ahn, I., and Choi, B. G. (2014). Northwest Africa 5738: Multistage fluid-driven secondary alteration in an extraordinarily evolved eucrite. Geochimica et Cosmochimica Acta 141, 199–227. https://doi.org/10.1016/j.gca.2014.06.008

Warren, P. H., Isa, J., Ebihara, M., Yamaguchi, A., and Baecker, B. (2017). Secondary-volatiles linked metallic iron in eucrites: The dual-origin metals of Camel Donga. Meteoritics and Planetary Science 52, 737–761. https://doi.org/10.1111/MAPS.12827

Wasson, J. T., Schaudy, R., Bild, R. W., and Chou, C. L. (1974). Mesosiderites—I. Compositions of their metallic portions and possible relationship to other metal-rich meteorite groups. Geochimica et Cosmochimica Acta, 38(1), 135–149. https://doi.org/10.1016/0016-7037(74)90199-9

Yamaguchi, A., Taylor, G. J., and Keil, K. (1996). Global crustal metamorphism of the eucrite parent body. Icarus 124, 97–112. https://doi.org/10.1006/icar.1996.0192

Yamaguchi, A., Taylor, G.J., Keil, K. (1997). Metamorphic history of the eucritic crust of 4 Vesta. Journal of Geophysical Research 102, 381–386.

Yamaguchi, A., Okamoto, C., and Ebihara, M. (2006). The origin of FeNi-metals in eucrites and implication for impact history of the HED parent body. 37th Annual Lunar and Planetary Science Conference, p. 1678.

Yamaguchi, A., Barrat, J. A., Greenwood, R. C., Shirai, N., Okamoto, C., Setoyanagi, T., Ebihara, M., Franchi, I. A., and Bohn, M. (2009). Crustal partial melting on Vesta: Evidence from highly metamorphosed eucrites. Geochimica et Cosmochimica Acta 73, 7162–7182. https://doi.org/10.1016/j.gca.2009.07.037

Yamaguchi, A., Barrat, J. A., Ito, M., and Bohn, M. (2011). Posteucritic magmatism on Vesta: Evidence from the petrology and thermal history of diogenites. Journal of Geophysical Research E: Planets, 116, 8009. https://doi.org/10.1029/2010JE003753

Zhang, A. C., Wang, R. C., Hsu, W. B., and Bartoschewitz, R. (2013). Record of S-rich vapors on asteroid 4 Vesta: Sulfurization in the Northwest Africa 2339 eucrite. Geochimica et Cosmochimica Acta 109, 1–13. https://doi.org/10.1016/j.gca.2013.01.036

Zhang, A. C., Kawasaki, N., Bao, H., Liu, J., Qin, L., Kuroda, M., Gao, J. F., Chen, L. H., He, Y., Sakamoto, N., and Yurimoto, H. (2020). Evidence of metasomatism in the interior of Vesta. Nature Communications 11, 1–7. https://doi.org/10.1038/s41467-020-15049-7